KSCE Journal of Civil Engineering (2022) 26(1):207-220
DOI 10.1007/s12205-021-2103-5

pISSN 1226-7988, eISSN 1976-3808
www.springer.com/12205

Structural Engineering

Analysis of Bearing Capacity of Circular Concrete Filled CFRP-Steel Tubular Beam-Column

Kuan Peng[a], **Yongbo Shao**[b], **and Qingli Wang**[c,d]

[a]*School of Mechatronic Engineering, Southwest Petroleum University, Chengdu 610500, China*
[b]*School of Civil Engineering and Geomatics, Southwest Petroleum University, Chengdu 610500, China*
[c]*School of Civil Engineering, University of Science and Technology Liaoning, Anshan 114051, China*
[d]*School of Civil Engineering, Shenyang Jianzhu University, Shenyang 110168, China*

ARTICLE HISTORY

Received 1 January 2021
Revised 19 May 2021
Accepted 12 August 2021
Published Online 9 October 2021

KEYWORDS

Circular CFRP-steel tube
In-filled concrete specimens
Static performance
Bearing capacity
Parametric study

ABSTRACT

In practice, it is common for circular concrete-filled CFRP-steel tube (C-CF-CFRP-ST) member severing under eccentric load, but there are few related investigations on its mechanical behavior currently. In this study, experimental study and finite element analysis are employed to reveal the static behavior of circular concrete filled CFRP-steel tube under eccentric compression. Total 32 C-CF-CFRP-ST specimens, taking the slenderness ratio (λ) and eccentric ratio (e) as principal parameters, were designed and tested firstly, obtaining the failure modes, N-u_m curve and the strains in the steel tube and CFRP. It was found that the damage of concrete became more serious with the decrease of the slenderness ratio but got mitigated with the increase of eccentricity. Additionally, it was indicated that the N-u_m curve of C-CF-CFRP-ST consisted of three stages, namely elastic stage, elastic-plastic stage and plastic stage. In the elastic-plastic stage, the damage is gradually accumulated in CFRP and concrete, and the specimens finally exhibited ductile failure in the end of plastic stage. In the entire loading process, CFRP has almost same strains compared to the steel tube. Following the experimental study, finite element analysis was conducted to investigate the static behavior of C-CF-CFRP-ST comprehensively. The proposed finite element model reproduced the compressive behavior of C-CF-CFRP-ST, in terms of failure modes and N-u_m curves. The influence of material strength, layers of CFRP and steel ratio on the static behavior of C-CF-CFRP-ST specimens were then studied through numerical parametric study. In the end, equations for predicting the bearing capacity of C-CF-CFRP-ST are proposed, and the predicted static strengths of the specimens are basically consistent with the experimental results.

1. Introduction

Due to the advantage of high strength of concrete material in tri-axial compression, Concrete-Filled Tubular (CFT) structure, in which concrete is confined by the outer tube, has wide applications in civil engineering. Traditional CFT structures include Concrete-Filled Steel Tubular (CFST) structure and the Concrete-Filled Fiber Reinforced Plastic Tubular (CF-FRP-T) structure. The two kinds of traditional CFT structures were studied by Han (2004) systematically. However, the durability and the bearing capacity of CFST members are susceptible to corrosive environment. CFRP (carbon fiber reinforced polymer) has good properties including light weight, high strength and good corrosion resistance, and therefore it can be employed to improve the performance of CFST structures, namely Concrete-Filled Carbon Fiber Reinforced Polymer-Steel Tubular structure (Wang and Shao, 2014). It is a new type of composite structure which combines the advantages of CFST and CFRP. The existence of CFRP can improve the bearing capacity and durability of CFST, and CFRP can also delay the buckling deformation of the steel tube.

Park (2010) investigated the behavior of square concrete filled CFRP-steel tubes under compression and cyclic load and found that the CFRP generally fractured at the corner of specimen during loading. Sundarraja and Ganesh (2010, 2011) found that the steel ratio and the number of CFRP layers have great influence on the bearing capacity of square CFRP-CFST specimens and proposed a

CORRESPONDENCE Yongbo Shao ybshao@swpu.edu.cn School of Civil Engineering and Geomatics, Southwest Petroleum University, Chengdu 610500, China

finite element simulation method to reproduce the mechanical behavior of square CFRP-CFST effectively. Tao et al. (2007, 2011) indicated that the bearing capacity of CFRP-CFST specimens was significantly reduced after fire, but the fire resistance ability of concrete filled CFRP-steel tube specimens was better than that of ordinary concrete filled steel tube specimens. Wang and Shao (2014) studied the influence of various materials on the bearing capacity of square concrete filled CFRP-steel tube under axial compression. Wang et al. (2015) and Feng et al. (2017) studied the influence of slenderness ratio and eccentric ratio on the performance of square concrete filled CFRP-steel tube. For the investigations on the circular concrete filled CFRP-steel tube, Che et al. (2012) and Choi (2010) studied the static performance of circular concrete filled CFRP-steel tube specimens under axial compression. Hu et al. (2011) investigated the compressive performance of FRP-confined circular concrete-filled thin steel tube. Guo et al. (2007) revealed the influence of CFRP layers and steel ratio on the performance of circular concrete filled CFRP-steel tube specimens.

Due to the lack of research on CF-CFRP-ST structure at this stage, the design method is not mature, and most of the previous studies were mainly focused on the axial compressive performance and the flexural performance of concrete filled CFRP-steel tube. In practice, it is common for concrete filled CFRP-steel tube subjected to bending moment besides axial compression. These difficulties make it less applied in engineering. Hence, it is necessary to carry out related research to reveal the mechanical behavior of CFRP-CFST beam-columns under eccentric loading condition.

In this paper, static behavior of circular CF-CFRP-ST beam-column specimens through both experimental tests and numerical simulations. Total 32 C-CF-CFRP-ST specimens, taking the slenderness ratio (λ) and eccentric ratio (e) as principal parameters, are designed and tested firstly, obtaining the failure modes, N-u_m curve and the strains in the steel tube and CFRP. Then, FE analysis will be conducted to study the static behavior of C-CF-

Table 1. Dimensions and Material Properties of Specimens

No.	Specimens	L (mm)	λ	e_0 (mm)	t_s (mm)	f_y (MPa)	f_u (MPa)	v_s	E_s (GPa)	f_{cu} (MPa)	f_{ck} (MPa)	$N_{bc}{}^{l}$ (kN)
1	CBC A-20	400	12	20	5	303	465	0.27	216	59.5	39.9	1232
2	CBC A-40	400	12	40	5	303	465	0.27	216	59.5	39.9	899.1
3	CBC A-60	400	12	60	5	303	465	0.27	216	59.5	39.9	672
4	CBC A-80	400	12	80	5	303	465	0.27	216	59.5	39.9	531.5
5	CBC B-20	530	16	20	5	303	465	0.27	216	59.5	39.9	1206.2
6	CBC B-40	530	16	40	5	303	465	0.27	216	59.5	39.9	881.1
7	CBC B-60	530	16	60	5	303	465	0.27	216	59.5	39.9	655.7
8	CBC B-80	530	16	80	5	303	465	0.27	216	59.5	39.9	525
9	CBC C-20	600	18	20	4.5	333	474	0.26	204	55.5	37.2	1164.7
10	CBC C-40	600	18	40	4.5	333	474	0.26	204	55.5	37.2	851.6
11	CBC C-60	600	18	60	4.5	333	474	0.26	204	55.5	37.2	635.9
12	CBC C-80	600	18	80	5	303	465	0.27	216	59.5	39.9	521.7
13	CBC D-20	800	24	20	4.5	333	474	0.26	204	55.5	37.2	1114.1
14	CBC D-40	800	24	40	4.5	333	474	0.26	204	55.5	37.2	809.8
15	CBC D-60	800	24	60	4.5	333	474	0.26	204	55.5	37.2	605.2
16	CBC D-80	800	24	80	5	303	465	0.27	216	59.5	39.9	484.2
17	CBC E-20	1,200	36	20	4.5	333	474	0.26	204	55.5	37.2	995.5
18	CBC E-40	1,200	36	40	4.5	333	474	0.26	204	55.5	37.2	724
19	CBC E-60	1,200	36	60	4.5	333	474	0.26	204	55.5	37.2	544
20	CBC E-80	1,200	36	80	5	303	465	0.27	216	59.5	39.9	468
21	CBC F-20	1,800	54	20	4.5	333	474	0.26	204	55.5	37.2	819
22	CBC F-40	1,800	54	40	4.5	333	474	0.26	204	55.5	37.2	601.1
23	CBC F-60	1,800	54	60	4.5	333	474	0.26	204	55.5	37.2	458.8
24	CBC F-80	1,800	54	80	5	303	465	0.27	216	59.5	39.9	370.4
25	CBC G-20	2,400	72	20	5	303	465	0.27	216	59.5	39.9	674.5
26	CBC G-40	2,400	72	40	5	303	465	0.27	216	59.5	39.9	504.8
27	CBC G-60	2,400	72	60	5	303	465	0.27	216	59.5	39.9	395.1
28	CBC G-80	2,400	72	80	5	303	465	0.27	216	59.5	39.9	320.7
29	CBC H-20	3,000	90	20	5	303	465	0.27	216	59.5	39.9	553.1
30	CBC H-40	3,000	90	40	5	303	465	0.27	216	59.5	39.9	423.3
31	CBC H-60	3,000	90	60	5	303	465	0.27	216	59.5	39.9	338.1
32	CBC H-80	3,000	90	80	5	303	465	0.27	216	59.5	39.9	277.1

CFRP-ST comprehensively based on the validated simulation method proposed in this study. Equations will be proposed to estimate the bearing capacity of the C-CF-CFRP-ST under eccentric load base on the numerical parametric analysis results.

2. Experimental Investigation

2.1 General

The slenderness ratio (λ) and the eccentricity ratio (e) are two principal parameters in the design of the specimens. The slenderness ratio (λ) of C-CF-CFRP-ST specimen is defined as follows:

$$\lambda = \frac{4L}{D}, \tag{1}$$

where L is the effective length of the specimen, D is the diameter of the steel tube. In this study, the value of D is 133 mm for all the tested specimens.

The eccentricity ratio (e) is defined as follows:

$$e = \frac{e_0}{r_e}, \tag{2}$$

where e_0 is the eccentric distance of load, r_c is the radius of the concrete.

The detailed parameters of all C-CF-CFRP-ST specimens are listed in Table 1, in which t_s is the thickness of the steel tube wall; f_y, f_u, v_s and E_s are the yield strength, the ultimate strength, the Poisson's ratio, and the elastic modulus of steel material, respectively; f_{cu} is the compressive strength of concrete, f_{ck} is the characteristic compressive strength of concrete (f_{ck} is taken as 0.67 f_{cu}). $N_{bc}{}^{t}$ is the bearing capacity of circular concrete filled CFRP steel tubular specimens measured in tests.

The relationship between the stability coefficient (φ) and the slenderness ratio of CF-CFRP-ST members can be depicted by Eq. (3), as shown in Fig. 1 (Wang and Shao, 2014):

$$\varphi = \begin{cases} 1 & (\lambda \le \lambda_p) \\ a\lambda^2 + b\lambda + c & (\lambda_0 < \lambda \le \lambda_p) \\ \dfrac{d}{(\lambda+35)^2} & (\lambda_p < \lambda) \end{cases}. \tag{3}$$

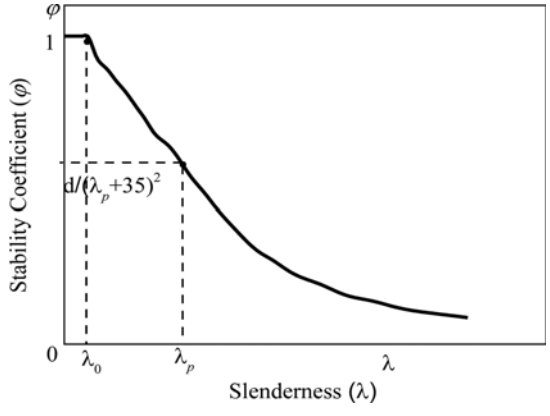

Fig. 1. The Relationship between the Stability Coefficient and Slenderness Ratio of CF-CFRP-ST Member

It is used to show the functional relationship between axial compression and slenderness. The coefficients in the expression of φ can be calculated from Eqs. (4) to (11):

$$a = \frac{[1+(35+2\lambda_p-\lambda_0)(-d/(\lambda_p+35)+2\lambda_p-\lambda_0)^3]}{(\lambda_p-\lambda_0)^2}, \tag{4}$$

$$b = \frac{d}{(\lambda_p+35)^3} - 2a\lambda_p, \tag{5}$$

$$c = 1 - a\lambda_0^2 - b\lambda_0, \tag{6}$$

$$d = \left[13000 + 4657 In\left(\frac{235}{f_y}\right)\right]\left(\frac{25}{f_{ck}+5}\right)^{0.3}\left(\frac{\alpha}{0.1}\right)^{0.05}(1+\eta)^{0.9}, \tag{7}$$

$$\begin{cases} \lambda_0 = \pi\sqrt{\dfrac{(420\zeta+550)}{[1.14+1.02(\zeta+3\zeta_{cf})]}\dfrac{f_{ck}}{}} \\ \lambda_p = \dfrac{1743}{\sqrt{f_y}} \end{cases}, \tag{8}$$

$$\xi_s + \xi_{cf} = \xi, \tag{9}$$

$$\xi_{cf} = \frac{A_{cft} f_{cft}}{(A_c f_{ck})}, \tag{10}$$

$$\xi_s = \frac{A_s f_y}{A_c f_{ck}}, \tag{11}$$

where A_s is the cross-sectional area of the concrete. A_c is the cross-sectional area of the steel tube; ξ_{cf} is the confinement factor of the CFRP; ξ is the confinement factor of specimen, ξ_s is the confinement factor of the steel tube; A_{cft} is the cross-sectional area of the transverse CFRP; the ultimate tensile strength of the transverse CFRP is defined as f_{cft}.

2.2 Material Properties and Specimen Preparations

Some specified parameters of the steel tubes are shown in Table 1. Cement, sand, water and coarse aggregate are used as raw materials of concrete. The mixed ratio of cement, sand, water and coarse aggregate is 485: 703: 150: 1062. f_{cu} is obtained from the compressive tests of concrete cubes with dimension of 150 mm × 150 mm × 150 mm. The elastic modulus (E_c) and the Poisson's ratio (v_c) of the concrete are assumed to be 35.9 GPa and 0.22 (Han, 2004), respectively. The properties of CFRP were measured from tensile test of coupons. The tensile strength (f_{cu}') and the elastic modulus (E_{cf}) of CFRP are 4.83 GPa and 230 GPa, respectively. The elongation percentage (δ_{cf}) of CFRP is 21.0%. The density of the carbon fiber sheet (w_{cf}) is 200 g·m^{-2}, and the thickness of a single layer carbon fiber sheet (t_{cf}) is 0.111 mm. For all the tested C-CF-CFRP-ST specimens, two layers of CFRP are bonded on outer surface of steel tube. The fiber directions of the first layer and the second layer of CFPR are in the axial direction and in the circumferential direction of the specimen, respectively.

2.3 Test Setup and Instrumentation

Figure 2 presents the instrument used for the static tests of C-CF-

CFRP-ST specimens. During tests, the eccentric load is applied on the specimen in several stages. In the initial stage of experimental tests, a loading increment of 1/10 of the bearing capacity N_{bc} predicted preliminary from an equivalent estimation method (Wang et al., 2015) is applied on specimen progressively. In the equivalent estimation method, the CFRPs are converted into an equivalent steel tube wall based on the same confinement strength. In this way, the strength estimation equations for concrete filled steel tube can be used for the bearing capacity calculation of C-CF-CFRP-ST specimens. It should be noted that the longitudinal CFRP is not involved in the conversion due to its negligible confining effect. When the applied load is about 60% of the predicted bearing capacity, the loading interval between two steps is changed to 1/15 – 1/20 of the predicted bearing capacity. When the deflection of specimen at the mid-span exceeds $L/50$, displacement control is adopted until failure. For each loading step, the applied load is kept for 2 to 3 minutes.

As shown in Fig. 2, five displacement sensors are pasted to monitor the deflection. Sixteen strain gauges are pasted at eight points (points 1 – 8) of both steel tube and CFRP laminates at the mid-height of the specimens, as illustrated in Fig. 3. At points 1, 3, 5 and 7, the circumferential strains of steel tube and CFRP are measured. At points 2, 4, 6 and 8, the axial strains of steel tube and CFRP are monitored.

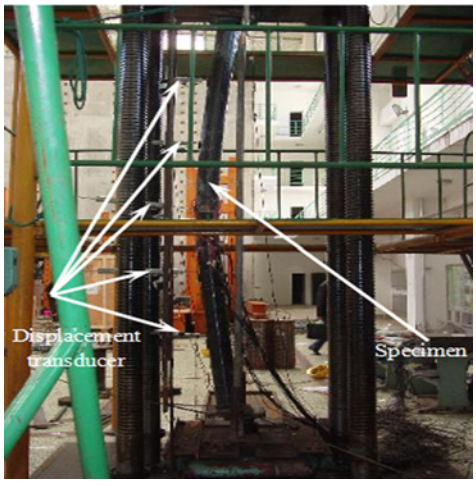

Fig. 2. Test Arrangement (Specimen CBC H-20)

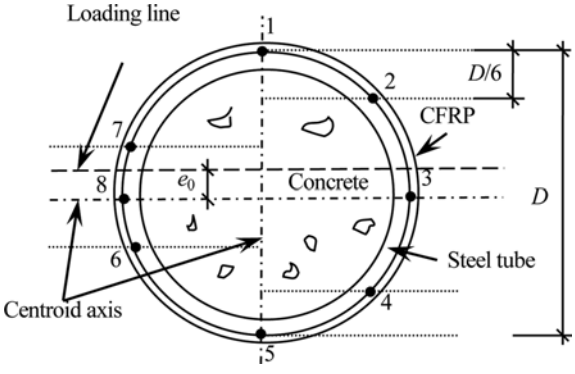

Fig. 3. Location of Strain Gauges

2.4 Observations during Tests

From the test results, both the slenderness ratio and the eccentricity ratio are found to have effect on the failure mode of specimens. For specimens with small slenderness ratio, the failure mode tends to be yielding failure. For specimens with small eccentricity ratio, the transverse CFRP in the compression zone fractures firstly, as shown in Fig. 4(a). As the deflection further increases, the longitudinal CFRP starts to fracture in the tensile zone, as shown in Fig. 4(b). As the eccentricity ratio increases, the longitudinal CFRP in the tensile zone fractures firstly. When the applied load drops to about 0.9 $N_{bc}{}^{t}$, the transversal CFRP begins to fracture. It should be noted that $N_{bc}{}^{t}$ is the measured bearing capacity of the C-CF-CFRP-ST specimen.

For specimens with large slenderness ratio, the failure mode tends to be global buckling. The fracture of longitudinal CFRP occurs in tensile zone with the increase of deflection for the specimen. The fracture of transversal CFRP only appears under the load with small eccentricity ratio. It is worthy to note that both the longitudinal and the transversal CFRPs of the specimens with large slenderness ratio and eccentricity ratio remain intact relatively even at large deflection. The failure modes of part of the tested specimens are presented in Fig. 5. It can be seen that the deflection of specimen is almost in arc shape.

Figure 6 shows the damage of concrete in tension and in compression zones. For specimens with the same eccentricity ratio, the damage of concrete is more severe with the decrease of slenderness ratio. The macroscopic expression is wide cracks in the tensile zone of concrete, as shown in Fig. 6(a). The crushing of concrete in the compression zone is shown in Fig. 6(b). The

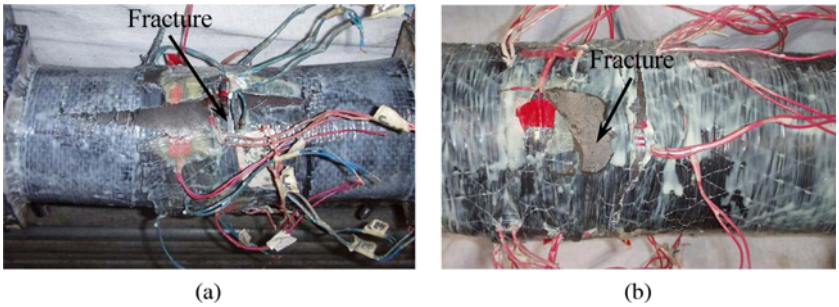

Fig. 4. Fracture of CFRP: (a) Fracture of Transverse CFRP, (b) Fracture of Longitudinal CFRP

(a) (b)

Fig. 5. Several Specimens after Testing: (a) Specimens of $\lambda = 90$, (b) Specimens of e = 1.3

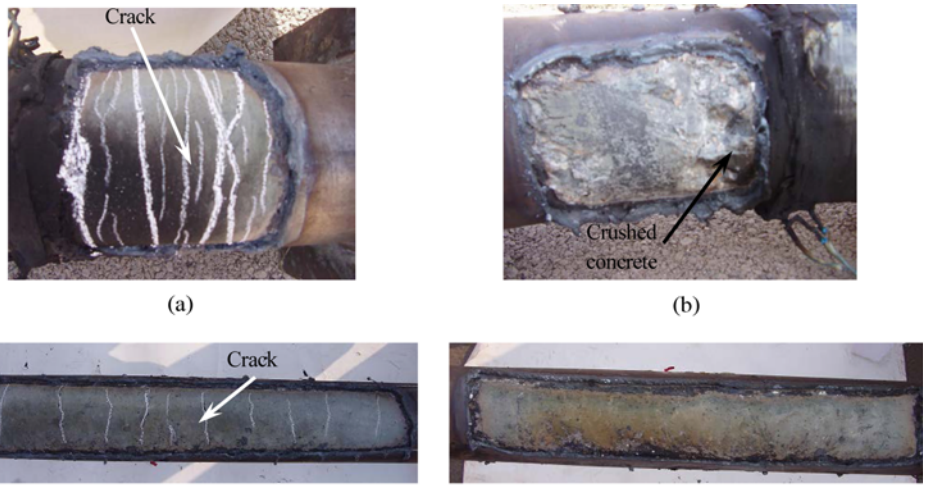

(a) (b) (c) (d)

Fig. 6. Failure Modes of Concrete inside Specimens: (a) Concrete in Tension Zone of CBC A-80, (b) Concrete in Compression Zone of CBC A-80, (c) Concrete in Tension Zone of CBC H-80, (d) Concrete in Compression Zone of CBC H-80

Table 2. Summary of Test Observation

Evaluating Indicator	Small eccentricity ratio	Large eccentricity ratio
Small slenderness ratio (The failure modes tend to be yield failure)	The transverse CFRP in the compression zone fractures firstly. Due to the increase of deflection, the longitudinal CFRP starts to fracture in the tensile zone. The damage of concrete is more serious.	The longitudinal CFRP in the tensile zone fractures firstly.
Large slenderness ratio (The failure modes tend to be instability state, and there are no obvious characteristics of strength failure)	The fracture of longitudinal CFRP is caused in tensile zone with the increase of deflection, and the transverse CFRP fractures. The concrete is slightly damaged.	The longitudinal CFRP in the tensile zone is not fractured even at large deflection after $N_{bc}{}^{l}$. The macroscopic expression is the wide cracks in the tensile zone of concrete.

damage level of concrete is mitigated with the increase of slenderness ratio, as shown in Fig. 6(c). Only tiny cracks occur in the tension zone of concrete, and compression zone of concrete is slightly damaged, as shown in Fig. 6(d). For the specimens with the same slenderness ratio, the damage of concrete is relatively minor for the specimen with large eccentricity ratio compared with the one with small eccentricity ratio, showing narrow cracks in the tensile zone of concrete.

All the experimental phenomena observed during test are summarized in Table 2.

2.5 Experiment Results and Analyses

2.5.1 Curve of Axial Compression-Deflection at Mid-height

The curves of N-u_m of all specimens are composed of three stages, namely elastic stage, elastic-plastic stage and plastic stage, as shown in Fig. 7. In the early loading stage, both the applied loads and the deflection are small, and the curves are approximately linear in elastic stage. Thereafter, the curves reach elastic-plastic stage. After $N_{bc}{}^{l}$ is reached, the axial compression is dropped in the curves, and the deflection increases rapidly with a gradual

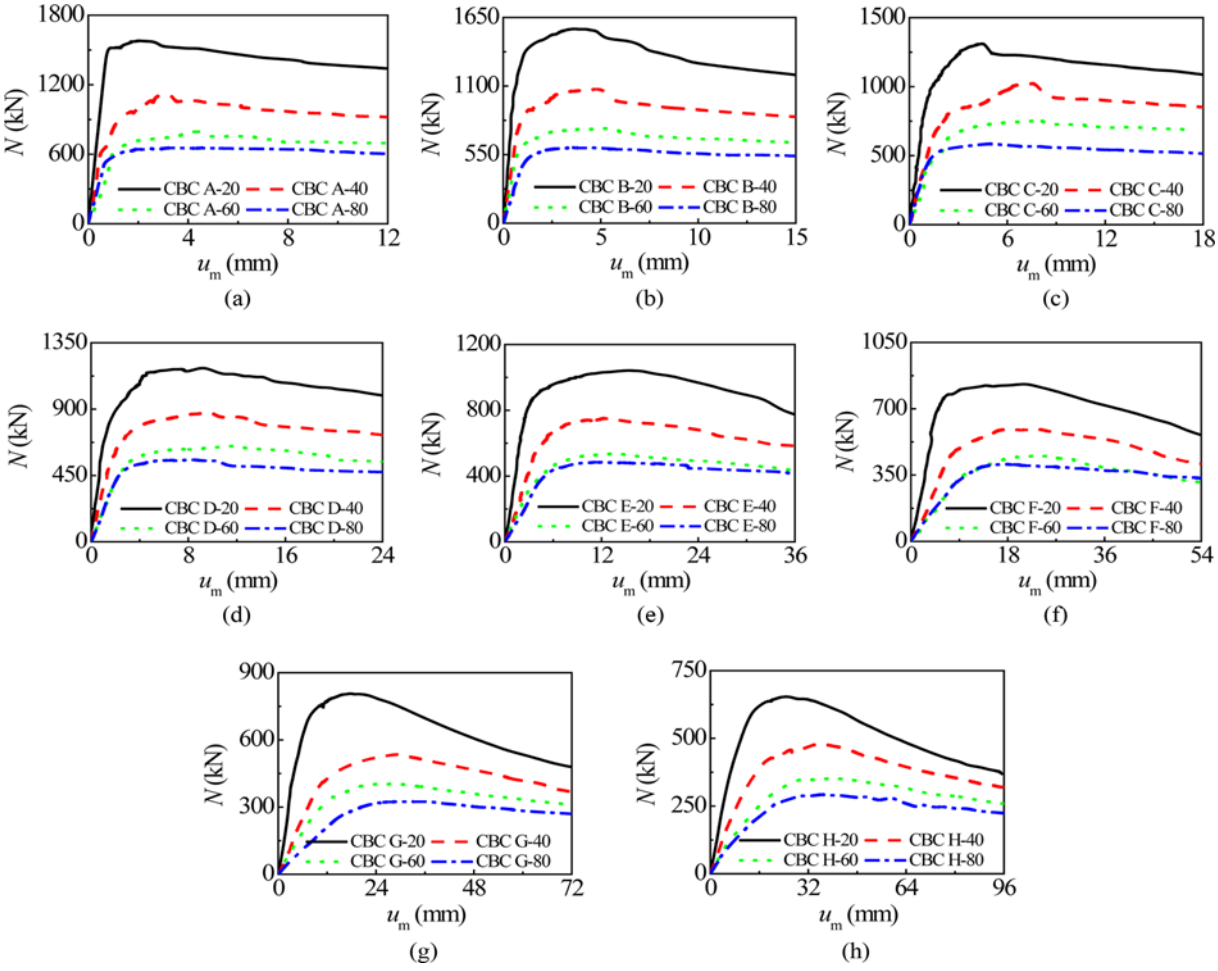

Fig. 7. The Curves of N-u_m of C-CF-CFRP-ST Specimens: (a) Specimens of $\lambda = 12$, (b) Specimens of $\lambda = 16$, (c) Specimens of $\lambda = 18$, (d) Specimens of $\lambda = 24$, (e) Specimens of $\lambda = 36$, (f) Specimens of $\lambda = 54$, (g) Specimens of $\lambda = 72$, (h) Specimens of $\lambda = 90$

dropping of loading. The experimental phenomena show that the failure of specimens at this stage is ductile.

2.5.2 Longitudinal Stain and Transverse Strain

Figure 8 shows $\varepsilon_{sl} - \varepsilon_{st}$ curve of specimen CBC H-20. ε_s is the strain measured at steel tube. ε_{sl} and ε_{st} are the longitudinal and the transverse strains of the steel tube, respectively. Positive strain denotes the steel tube under compression. Otherwise, the steel tube is under tension.

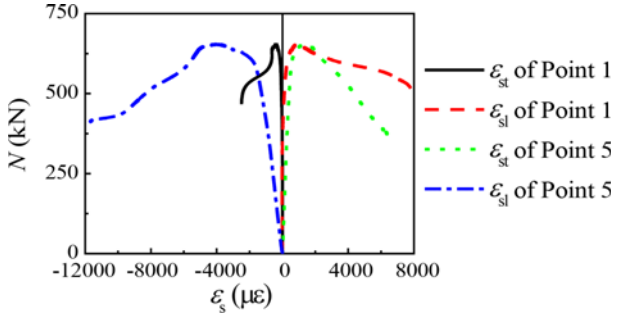

Fig. 8. Contrast between ε_{st} and ε_{sl} of Point 1 – 5 for Specimen CBC H-20

It is found that ε_{sl} and ε_{st} have opposite signs at the same point. As shown in Fig. 8, the transversal strain ε_{st} at point 5 is positive, indicating the steel tube sustaining compressive stress. In this situation, there is no confinement from the steel tube to the infilled concrete for the specimen CBC H-20.

2.5.3 Plane Section Assumption

Figure 9 shows the measured ε_{sl} at the middle-height of the C-CF-CFRP-ST specimens with λ equal to 90. Along the radial direction of the circular section, the strains show linear distribution, indicating the rigid rotation of the cross-section at the middle-height of the specimen approximately. In view of this phenomena, the it can be concluded that plane section assumption is applicable for the C-CF-CFRP-ST specimens under eccentric load.

2.5.4 Comparison of Strain Measured at the Steel Tube and the CFRP

The strains measured at steel tube are compared with that of CFRP in Fig. 10. It should be noted that ε_l is the longitudinal

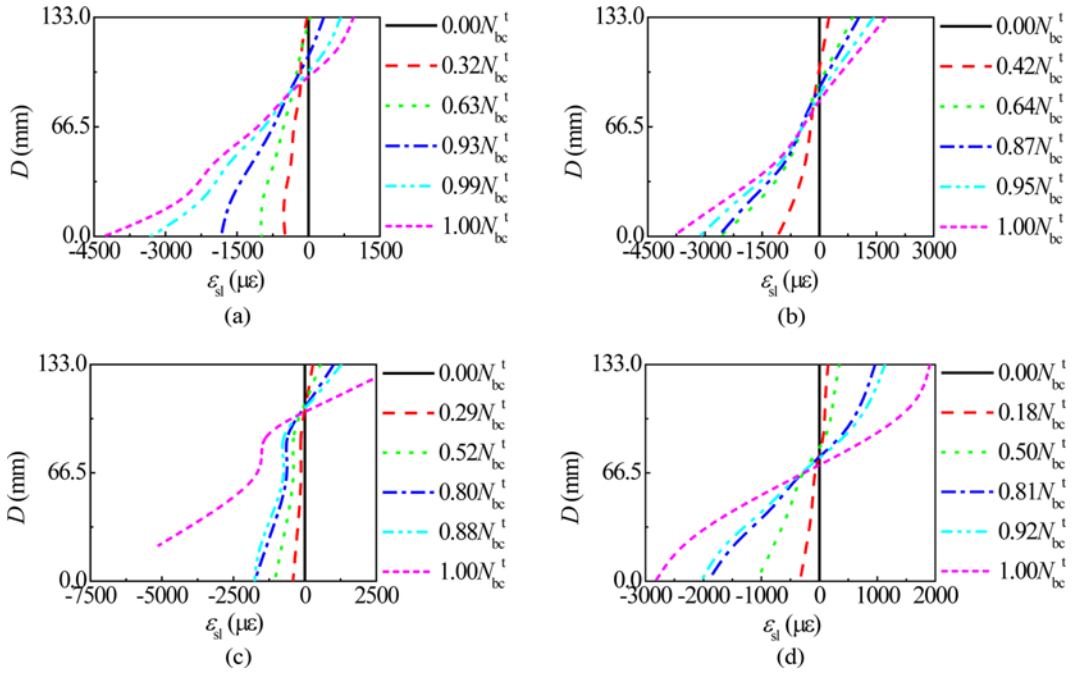

Fig. 9. Distribution of ε_{sl} over Depth of Mid-height Cross-Section of Specimens of $\lambda = 90$: (a) Specimen CBC H-20, (b) Specimen CBC H-40, (c) Specimen CBC H-60, (d) Specimen CBC H-80

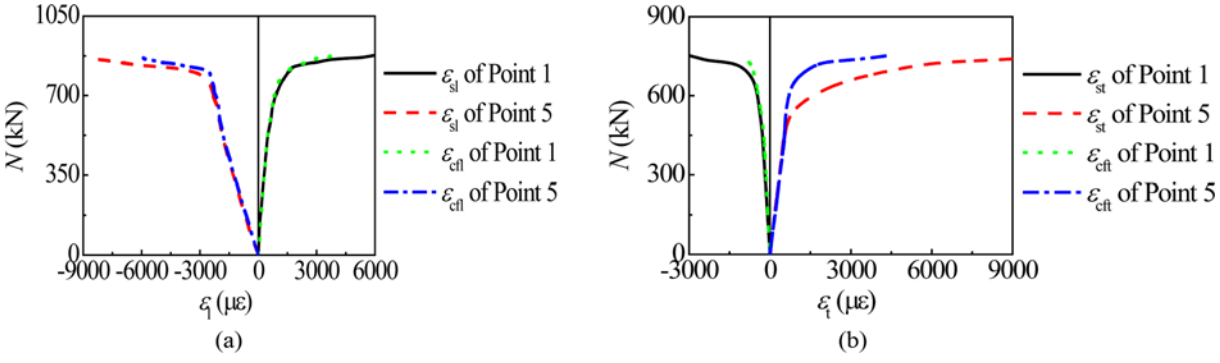

Fig. 10. Contrast of ε_s and ε_{cf} between Steel Tube and CFRP: (a) N-ε_t Curves of Specimen CBC D-40, (b) N-ε_t Curves of Specimen CBC C-60

strain; ε_t is the transverse strain; ε_{cfl} is the longitudinal strain of CFRP; ε_{cft} is the transverse strain of CFRP. As shown in Fig. 10, the strains of CFRP and steel tube remain almost consistent in both transverse and longitudinal directions.

3. Finite Element Simulation

3.1 Stress-Strain Relationship of Materials

To further analyze the mechanical behavior of C-CF-CFRP-ST specimens under eccentric load comprehensively, Finite element models are established and analyzed in this study. The details of the stress-strain relationships of the steel are determined according to the constitutive model suggested by Han et al. (2001). The Concrete Damage Plasticity is used in the finite element simulation of concrete, and stress-strain of concrete relationship is shown in Eq. (12) (Wang et al., 2016):

$$\sigma_{cl}/\sigma_0 = \begin{cases} 2\left(\frac{\varepsilon_{cl}}{\varepsilon_0}\right) - \left(\frac{\varepsilon_{cl}}{\varepsilon_0}\right)^2 & (\varepsilon_{cl} \le \varepsilon_0) \\ \begin{cases} \left[1 - q + q\left(\frac{\varepsilon_{cl}}{\varepsilon_0}\right)^{0.1\xi}\right]\left(\frac{\varepsilon_{cl}}{\varepsilon_0}\right)^C & (\varepsilon_S \ge 1.12) \\ \dfrac{\left(\frac{\varepsilon_{cl}}{\varepsilon_0}\right)^{1+D}}{\beta\left(\frac{\varepsilon_{cl}}{\varepsilon_0} - 1\right)^2 + \frac{\varepsilon_{cl}}{\varepsilon_0}} & (\varepsilon_S < 1.12) \end{cases} & (\varepsilon_0 < \varepsilon_{cl} \le \varepsilon_u), \\ \dfrac{\frac{\varepsilon_{cl}}{\varepsilon_0}}{\beta_S\left(\frac{\varepsilon_{cl}}{\varepsilon_0} - 1\right)^2 + \frac{\varepsilon_{cl}}{\varepsilon_0}} & (\varepsilon_{cl} > \varepsilon_u) \end{cases} \tag{12}$$

$$\sigma_0 = f_c' \text{ (MPa)}, \tag{13}$$

$$\varepsilon_0 = \varepsilon_{cc} + (600 + 32.4 f_c')\xi^{0.2} \times 10^{-6}, \tag{14}$$

$$\varepsilon_{cc} = (1300 + 12.09 f_c') \times 10^6, \quad (15)$$

$$q = \frac{\xi^{0.745}}{2 + \xi}, \quad (16)$$

$$C = \zeta'(2.231 - 4.611\zeta'), \quad (17)$$

$$D = \zeta'(1.545 - 1.238\zeta'), \quad (18)$$

$$\beta = 3.28(2.36 \times 10^{-5})^{0.25 + (\xi - 0.5)^6} f_c'^2 \times 10^{-4}, \quad (19)$$

$$\beta_s = 0.5(2.36 \times 10^{-5})^{0.25 + (\xi_s - 0.5)^7} f_c' \times 10^{-4}, \quad (20)$$

$$\varepsilon_u = \varepsilon_0 + 51659\xi_{cf} - 38904\xi_{cf}^2, \quad (21)$$

where the compressive strength of the concrete is defined as f_c'. ξ' is the confinement factor ratio. q, C and D are related parameters about $\xi \cdot \beta$ and β_s are related parameters about $\xi_s \cdot \varepsilon_u$ is the longitudinal strain of the specimen.

The failure energy criterion of concrete is used to simulate the tension of concrete:

$$G_f = 40 + 4(f_c' - 20), \quad (22)$$

$$s_{t0} = 0.26(1.5 f_c')^{1.5}, \quad (23)$$

where the total energy consumed in concrete fracture process is defined as G_f; σ_{t0} is the ultimate tensile strength of concrete.

The shrinkage and the creep are not considered for concrete material in the finite element model. Yao (2006) found that shrinkage of concrete during 28 days of curing was very small, which can be ignored. The experimental tests in this study were carried out after 28 days of curing, so the shrinkage of concrete has very little effect on the results. Creep is generally the deformation of concrete in a non-solid state or long service time. Because the static tests are finished in a short time and the concrete was already cured for 28 days, the creep of concrete can be ignored.

The confinement of transverse CFRP is quantified by the confinement factor of transverse CFRP (ξ_{cf}) proposed by Che et al. (2012). The reinforcement efficiency of longitudinal CFRP is defined as a strengthening coefficient (η) proposed by Wang et al. (2016). All influence factors are given from Eqs. (24) to (26):

$$\eta = \frac{A_{cfl} f_{cfl}}{A_s f_y}, \quad (24)$$

$$f_{cft} = E_{cf} \varepsilon_{cftr}, \quad (25)$$

$$f_{cfl} = E_{cf} \varepsilon_{cflr}, \quad (26)$$

where A_{cft} and f_{cft} are the cross-sectional area and the ultimate tensile strength of the transverse CFRP, respectively. A_{cfl} and f_{cfl} are the cross-sectional area and the ultimate tensile strength of the longitudinal CFRP, respectively.

It has been verified by previous experiments that lateral restraint of CFRPs to the steel tube is lost once the fracture strain of transversal CFRP is reached (ε_{cftr} = 5,500 $\mu\varepsilon$). When the rupture strain of longitudinal CFRPs is reached (ε_{cflr} = 10,000 $\mu\varepsilon$), the longitudinal strengthening effect to the members is lost (Wang et al., 2016).

3.2 Finite Element Model

3.2.1 Division of Mesh and Interactions

The refined mesh method is used to analyze the mesh convergence before meshing. Because the pressure between steel tube and concrete can only be transferred on the surfaces of two materials, the hard contact mode is adopted between them. It is assumed

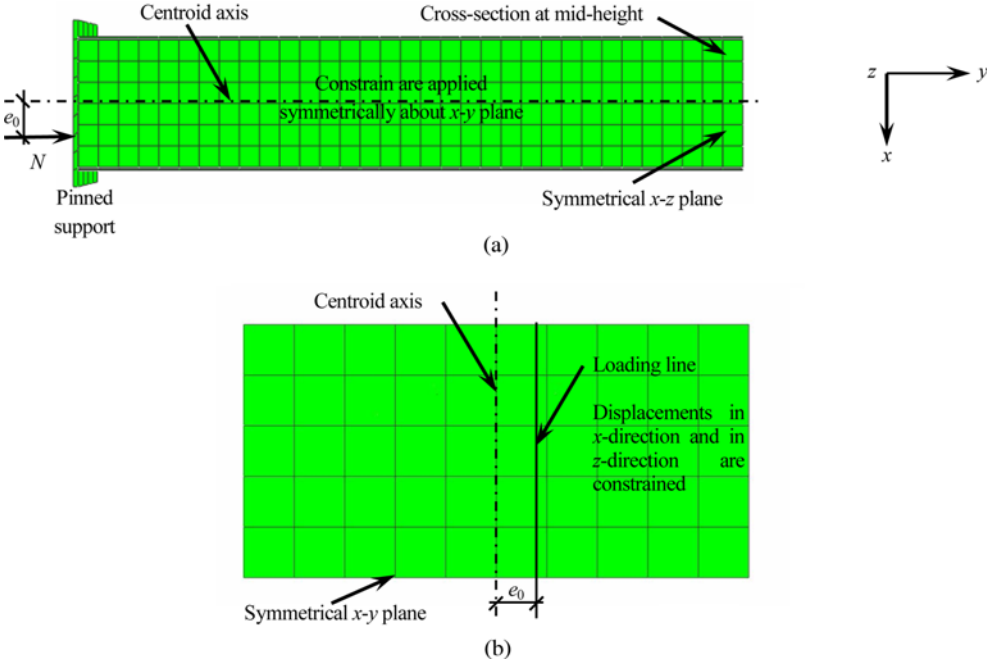

Fig. 11. Boundary Conditions: (a) Longitudinal Direction, (b) End Plate

that the steel tube and the end plate are integral part in the finite element model, so the element nodes of the steel tube and the end plate on the contact surface have the same nodal degree of freedom. In the finite element simulation, there is no slip in the tangential direction, and it is hard contact between the end plate and the concrete in the normal direction. According to the test results in Fig. 9, it can be seen that the strains of CFRP and steel tube remain consistent. Therefore, it is assumed that there is no slipping between CFRP and steel tube, and the two contact adopts bonding.

3.2.2 Boundary Conditions

Boundary conditions which used in the finite element analysis are same as those which used in the tests, as shown in Fig. 11. Because the geometry and boundary conditions are symmetrical, quarter of the whole model is selected to study. Symmetrical constraints are used to the symmetrical plane of the model. Displacements of directions of x, y and z are fixed at one end, and loads are applied at the other end. The incremental iteration method of displacement control is used in the finite element analysis.

3.3 FE Results

3.3.1 Deformed Modes

32 specimens by using the finite element models are studied. The failure modes and deformed modes of the tested specimens are simulated by the finite element models, as shown in Fig. 12. The

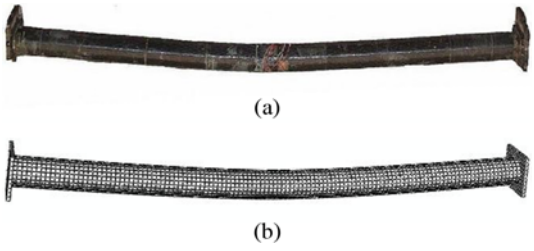

Fig. 12. Deformed Modes: (a) Experimental Result, (b) Simulated Result

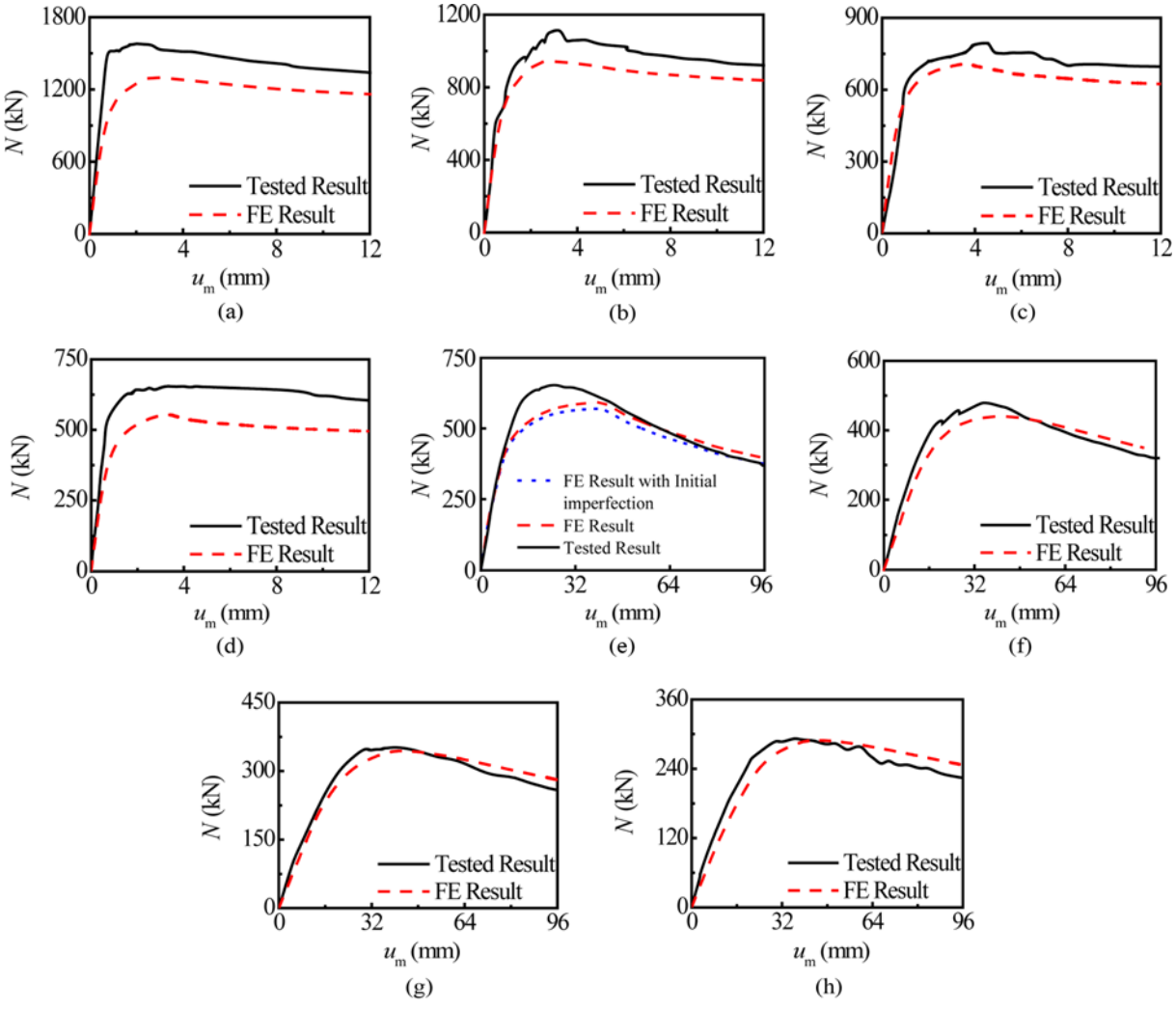

Fig. 13. Contrast of the Curves of N-u_m between FE Results and Tested Results: (a) Specimen CBC A-20, (b) Specimen CBC A-40, (c) Specimen CBC A-60, (d) Specimen CBC A-80, (e) Specimen CBC H-20, (f) Specimen CBC H-40, (g) Specimen CBC H-60, (h) Specimen CBC H-80

simulation results are in good agreement with the experimental results.

3.3.2 The Curves of N-u_m

Figure 13 shows the comparison of N-u_m curves from the FE results and the experimental results. From the comparison, the finite element results are basically consistent with the experimental results. In some investigations, it was revealed that the influence of initial imperfections on the bearing capacity of members. Aslani et al. (2015) studied such influence and found that the effect of the initial imperfection on the bearing capacity of composite columns can be ignored. However, Lu et al. (2020) showed that the influence of initial imperfections on the post buckling strength of CFST column with different width-thickness ratio is different. In addition, the influence of imperfection on the slender columns is more obvious compared with short column. To study the influence of initial imperfections on the finite element model of C-CF-CFRP-ST, specimen CBC H-20 is selected. Its width-thickness ratio and slenderness ratio are 26.6 and 90, respectively, and 90 is the maximum slenderness ratio in this experiment. According to Australian Standards, Eurocode 4, and American Institute of Steel Construction, the initial imperfections value equal to D/500 (Han et al., 2001) is assigned to the buckling mode. The effect of initial imperfection on N-u_m relationship curve of CBC H-20 specimen is illustrated in Fig. 13(e). It can be seen that the error between the N-u_m curves obtained from the models with and without initial imperfection defined, since the in-filled concrete mitigates buckling level and significantly increase the bearing capacity of the specimen. In addition, CFRP can delay the buckling deformation of members. Therefore, the influence of initial imperfection is ignored in the finite element model of C-CF-CFRP-ST.

4. Parametric Analyses

Based on the validated finite element simulation method, numerical parametric study is carried out to investigate the influence of principle factors on the mechanical behavior of C-CF-CFRP-ST specimens, including the loading path, the eccentric ratio, the slenderness ratio, the layers of the CFRPs, the yield strength of the steel tube, and the strength of concrete and the steel ratio ($\alpha = A_s/A_c$).

4.1 Influence of Loading Path

There are three different loading paths for specimens, as shown in Fig. 14. Loading path 1 is designed that the axial compression (N) is applied firstly and kept constantly, and then the bending moment (M) is applied. Loading path 2 is designed that the axial compression (N) and the bending moment (M) are applied simultaneously with a proportional increment. Loading path 3 is designed that the bending moment (M) applied firstly and kept it constantly, then the axial compression (N) is applied.

The N-M curve of specimens of C-CF-CFRP-ST is obtained by changing the loading mode in FE model, i.e., the loads are applied according to path 1 and path 2, respectively. Fig. 15 shows the N-M curves of loading path 1 and loading path 2. The results show that two different loading routes have slight effect on the bearing capacity of C-CF-CFRP-ST specimens.

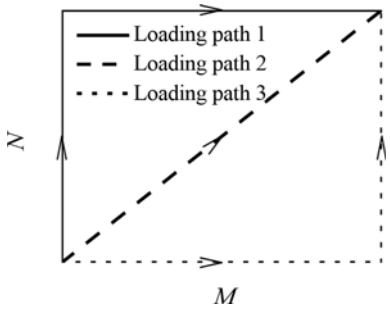

Fig. 14. Loading Paths of Specimens

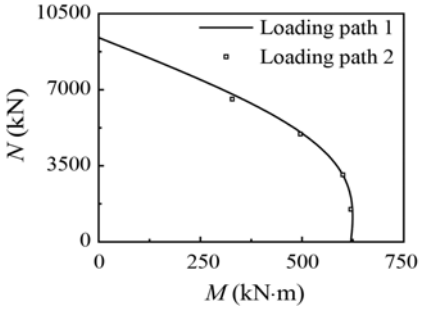

Fig. 15. N-M Curves under Different Loading Paths

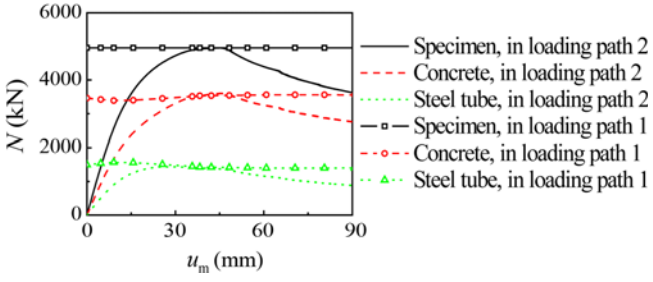

Fig. 16. Distributed Axial Loads of Overall Specimen, Steel Tube and Concrete Respectively during Loading Process under Different Loading Paths

For the loading path 1 and 2, the axial loads applied on specimen is the sum of the loads sustained by steel tube and concrete which can be exported from FE model directly. This result is shown in Fig. 16. The different axial loads are applied in the steel tube and the concrete under different loading paths. Although the loading paths are different, the sustained axial loads are almost same at the bearing capacity.

The longitudinal stress distributions on the cross-section of middle-height of concrete obtained from under same applied load (N = 4949.6 KN, M = 773.8 KN·m) but different loading paths are shown in Fig. 17. In the condition of the same bearing capacity, the distribution pattern and the value of the longitudinal stress are consistency under different loading paths.

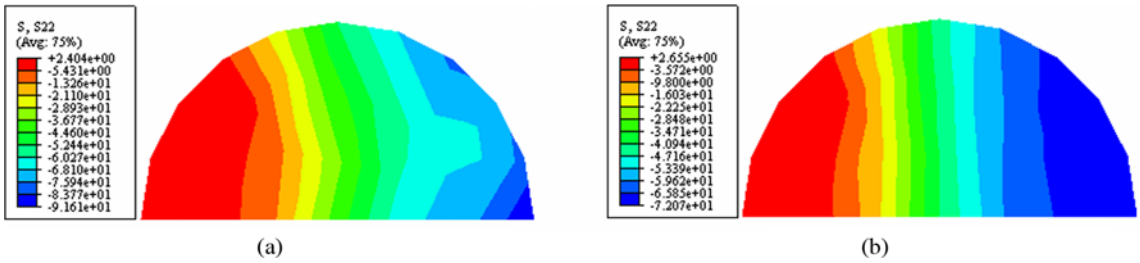

Fig. 17. The Longitudinal Stress Distributions on the Cross-Section of Middle-Height of Concrete Obtained from under Same Applied Load but Different Loading Paths: (a) Loading Path 1, (b) Loading Path 2

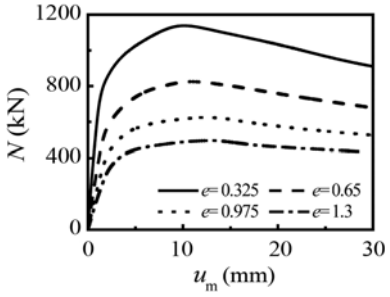

Fig. 18. Influence of Eccentric Ratio on the Curves of N-u_m of C-CF-CFRP-ST Specimens

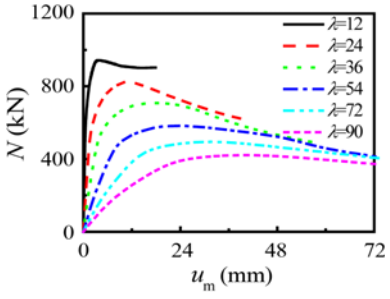

Fig. 19. Influence of Slenderness Ratio on the Curves of N-u_m of C-CF-CFRP-ST Specimens

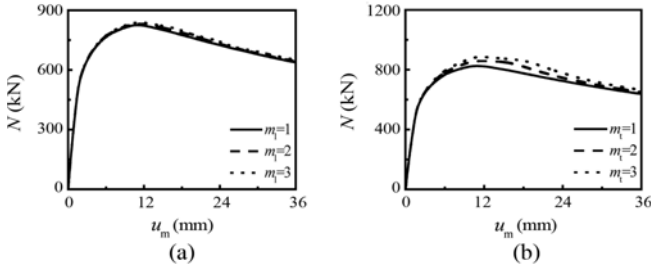

Fig. 20. Influence of Layers of CFRP on the Curve of N-u_m of C-CF-CFRP-ST Specimens: (a) m_l, (b) m_t

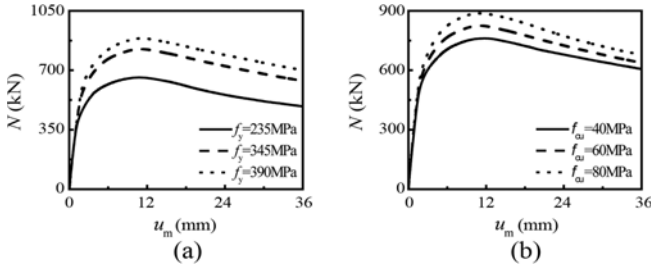

Fig. 21. Influence of Strengths of Materials on the Curves of N-u_m of C-CF-CFRP-ST Specimens: (a) f_y, (b) f_{cu}

4.2 Influence of Eccentric Ratio

Figure 18 shows the effect of eccentricity ratio on the N-u_m curves of C-CF-CFRP-ST specimens. It is found that the shape of the curves has no obvious variation with the increase of eccentricity ratio, while the stiffness of elastic stage and the load carrying capacity both decrease remarkably.

4.3 Influence of Slenderness Ratio

Figure 19 shows the effect of slenderness ratio on the of N-u_m curves of C-CF-CFRP-ST specimens. The stiffness of elastic stage and the load carrying capacity are reduced remarkably with the slenderness ratio increases, and the shape of the curves is changed as well.

4.4 Influence of Layers of CFRPs

Figure 20 shows the effect of layers of CFRPs on the specimens. m_l and m_t denote the number of longitudinal and transversal CFRP layers, respectively. With the increase of m_l, s the shape of N-u_m curve is slightly changed that the stiffness of the elastic stage and the bearing capacity of the specimens are increased slightly. In addition, with the increase of m_t, no significant change is observed in the overall shape of the curve and the stiffness of elastic stage, but the bearing capacity of the specimens is improved to a certain extent.

4.5 Influence of Strengths of Materials

The effect of strength of materials on the specimens is shown in Fig. 21. With the increase of f_y, the shape of the curves and the stiffness of the elastic stage have slight variation, and the bearing capacity of the specimens is significantly improved. In addition, bearing capacity of the specimens is improved continuously with the increase of f_{cu}, and the shape of the curves and the stiffness of the elastic stage have no obvious variation.

4.6 Influence of Steel Ratio

Figure 22 shows the effect of steel ratio on specimens. With the increase of α, the bearing capacity of the specimens is improved. The stiffness of curves is increased slightly at the elastic stage, but there is almost no change in curve shape.

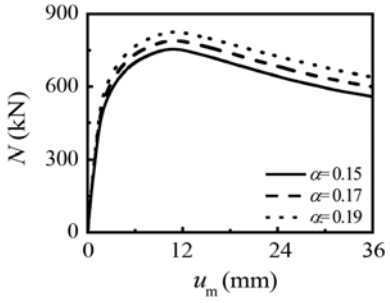

Fig. 22. Effect of Steel Ratio on the Curves of N-u_m of C-CF-CFRP-ST Specimens

5. Equations Carrying Capacity of Specimens of C-CF-CFRP-ST

5.1 Equations

Figure 23 shows the typical curve of $\frac{N_{bc}}{N_u}-\frac{M_{bc}}{M_u}$ for the specimens. N_u and N_{bc} are the axial compressive bearing capacity and the flexural of C-CF-CFRP-ST stub columns (Wang and Shao, 2015). M_u is defined as the flexural capacity of the C-CF-CFRP-ST specimens. M_{bc} is defined as the flexural capacity of the C-CF-CFRP-ST beam-columns (Li, 2016).

The experimental parameters are listed as follows: where f_y = 200 – 400 MPa, f_{cu} = 30 – 120 MPa, η = 0 – 0.9, E_s = 206 GPa, υ_s = 0.3, υ_c = 0.2, $E_c = 4{,}700 f_c'^{0.5}$ MPa, ξ_s = 0.2 – 4, ξ_{cf} = 0 – 0.6. The abscissa ζ_0 and the ordinate η_0 at point A in Fig. 23 can be expressed as a function about ξ (Zand et al., 2016; Zand et al., 2017):

$$\zeta_0 = 0.18\xi^{-1.15} + 1, \tag{27}$$

$$\eta_0 = \begin{cases} 0.5 - 0.245\xi & (\xi \le 0.4) \\ 0.1 + 0.14\xi^{-0.84} & (\xi > 0.4) \end{cases}. \tag{28}$$

The curve can be approximately divided into two stages and it can be described mathematically as follows:

Stage C ~ D ($\frac{N_{bc}}{N_u} \ge 2\eta_0$),

$$\frac{N_{bc}}{N_u} + a\frac{M_{bc}}{M_u} = 1, \tag{29}$$

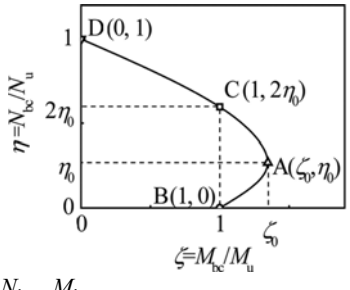

Fig. 23. Typical $\frac{N_{bc}}{N_u}-\frac{M_{bc}}{M_u}$ Curve

Stage C~A~B ($\frac{N_{bc}}{N_u} < 2\eta_0$)

$$-b\left(\frac{N_{bc}}{N_u}\right)^2 - C\frac{N_{bc}}{N_u} + \frac{M_{bc}}{M_u} = 1, \tag{30}$$

where $a = 1 - 2\eta_0$, $b = \frac{1-\zeta_0}{\eta_0^2}$ and $c = \frac{2(\zeta_0 - 1)}{\eta_0}$

Considering the effect of the slenderness ratio of the specimens (φ, stability coefficient of the C-CF-CFRP-ST) (Wang et al., 2016), the coupled equation $\frac{N_{bc}}{N_u}-\frac{M_{bc}}{M_u}$ of the C-CFRP-CFST specimens is obtained as follows:

$$\begin{cases} \frac{1}{\varphi}\frac{N_{bc}}{N_u} + \frac{a}{d}\frac{M_{bc}}{M_u} = 1 & \left(\frac{N_{bc}}{N_u} \ge 2\phi^3\eta_0\right) \\ -b\left(\frac{N_{bc}}{N_u}\right)^2 - C\frac{N_{bc}}{N_u} + \frac{M_{bc}}{M_u} = 1 & \left(\frac{N_{bc}}{N_u} < 2\phi^3\eta_0\right) \end{cases}, \tag{31}$$

where $a = 1 - 2\varphi^2\eta_0$, $b = \beta = \frac{1-\zeta_0}{\varphi^3\eta_0^2}$ and $c = \frac{2(\zeta_0-1)}{\eta_0}$, and d is an enlarged coefficient of the moment considering second order effect:

$$d = 1 - 0.4\frac{N}{N_E}, \tag{32}$$

where N_E is the critical buckling load calculated from Euler's equation:

$$N_E = \frac{\pi^2 E_{cfsc} A_{cfsc}}{\lambda^2}, \tag{33}$$

$$E_{cfsc} = \frac{f_{cfsp}}{\varepsilon_{cfscp}}, \tag{34}$$

$$f_{cfscp} = \left[\frac{0.192}{(1-0.6\xi_{cf})^2\left(\frac{f_y}{235}\right)} + 0.488(1-2.4\xi_{cf})f_{cfscy}\right], \tag{35}$$

$$f_{cfscy} = [1.14 + 1.02(\xi_s + 3\xi_{cf})]f_{ck}, \tag{36}$$

$$\varepsilon_{cfscp} = 3.25 \times 10^{-6} f_y, \tag{37}$$

where E_{cfsc} is the composite elastic modulus of the members, A_{cfsc} is the cross-sectional area of the members, f_{cfscp} and ε_{cfscp} are the nominal compressive proportional stress and its corresponding strain of specimens, f_{cfscy} is compressive strength in axial direction of specimens.

5.2 Validation of Presented Equations

Figure 24 shows the comparisons between the calculated results (N_{bc}^c) and the tested results (N_{bc}^t). The average value of $\frac{N_{bc}^c}{N_{bc}^t}$ is 0.935, and the mean square error is 0.109. It can be concluded

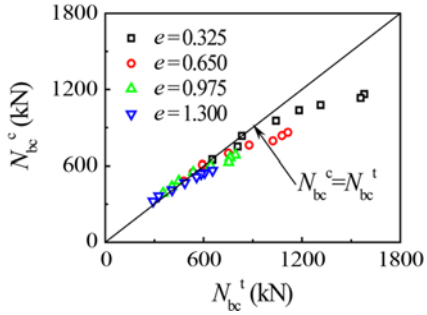

Fig. 24. Comparisons between $N_{bc}{}^{c}$ and N_b

that the calculated results agree well with the experimental results.

6. Conclusions

The static performance of the C-CF-CFRP-ST beam-columns is studied by experimental and numerical investigation. Firstly, total 32 C-CF-CFRP-ST specimens, taking the slenderness ratio (λ) and eccentric ratio (e) as principal parameters, are designed and tested, obtaining the failure modes, N-u_m curve and the strains in the steel tube and CFRP. Then, finite element analysis will be conducted to investigate the static behavior of C-CF-CFRP-ST comprehensively based on the validated simulation method proposed in this study. Finally, relying on the numerical parametric study results, equations will be proposed to estimate the bearing capacity of the C-CF-CFRP-ST under eccentric load. Based on the results from experimental study and numerical analysis, main conclusions are drawn as follows:

1. The N-u_m curves show that all specimens experience stage of elastic, stage of elastic-plastic and stage of softening, and the failure modes of the C-CF-CFRP-ST specimens are ductile.
2. In both longitudinal and transverse directions, the strains of CFRP and steel tube remain consistent during the loading process. The plane section assumption is application for mechanical behavior analysis of the C-CF-CFRP-ST specimens under eccentric load. In addition, the steel tube in longitudinal tensile zone has less transversal restraint effect on concrete.
3. The impact of loading path on the mechanical behavior of C-CF-CFRP-ST specimens can be neglected. The results of parametric analysis show that the bearing capacity of C-CF-CFRP-ST specimens can be significantly improved by increasing the concrete strength, steel yield strength and reinforcement ratio, while the increase of layer of longitudinal and transverse CFRP has slight effect on the bearing capacity. In addition, with the increase of steel ratio, the stiffness slightly increases in the elastic stage. The bearing capacity is significantly reduced with the increase of slenderness ratio or eccentricity ratio. The shape of curves of N-u_m is changed by the variation of load, stiffness in elastic stage and slenderness ratio.
4. Coupled equations for the bearing capacity of C-CF-CFRP-ST specimens are proposed and the equations are verified to be accurate. The verification results show that calculated results of the coupled equations agree well with the tested results, and the theoretical basis is provided by the equations for its application in practical engineering.

Acknowledgments

The research reported in the study is supported by Project for Talent of Liaoning Province of China (No. XLYC1902009), PHD Start-up Fund of Natural Science Foundation of Liaoning Province of China (20170520139) and Scientific Innovation Group for Youths of Sichuan Province of China (No. 2019JDTD0017).

ORCID

Not Applicable

References

Aslani F, Uy B, Tao Z (2015) Behaviour and design of composite columns incorporating compact high-strength steel plates. *Journal of Constructional Steel Research* 10(7):94-110, DOI: 10.1016/j.jcsr.2015.01.005

Che Y, Wang QL, Shao YB (2012) Compressive performances of the concrete filled circular CFRP-steel tube (C-CFRP-CFST). *Advanced Steel Construction* 8(4):311-338, DOI: 10.18057/IJASC.2012.8.4.2

Choi KK (2010) Analytical model of circular CFRP confined concrete-filled steel tubular columns under axial compression. *Journal of Composites for Construction* 14(1):125-133, DOI: 10.1061/(ASCE)CC.1943-5614.0000056

Feng ML, Wang QL, Shao YB (2017) Static behavior of axially compressed square concrete filled CFRP-steel tubular (S-CF-CFRP-ST) columns with moderate slenderness. *Thin-Walled Structure* 110(1):106-122, DOI: 10.1016/j.tws.2016.10.019

Guo LH, Zhang SH, Kim WJ, Ranzi G (2007) Behavior of square hollow steel tubes and steel tubes filled with concrete. *Thin-Walled Structures* 45(12):961-973, DOI: 10.1016/j.tws.2007.07.009

Han LH (2004) Behavior and calculation on concrete-filled steel CHS (circular hollow section) specimens. *Steel and Composite Structures* 4(3):169-188, DOI: 10.12989/scs.2004.4.3.169

Han LH, Zhao XL, Tao Z (2001) Tests and mechanics model of concrete-filled stub columns, columns and beam-columns. *Steel and Composite Structures* 1(1):51-74, DOI: 10.1296/SCS2001.01.01.04

Hu YM, Yu T, Teng JG (2011) FRP-confined circular concrete-filled thin steel tubes under axial compression. *Journal of Composites for Construction* 15(5):850-860, DOI: 10.1061/(ASCE)CC.1943-5614.0000217

Li DS (2016) Identification of failure mechanisms for CFRP-confined circular concrete-filled steel tubular columns through acoustic emission signals. *Smart Structures and Systems* 18(3):525-540, DOI: 10.12989/sss.2016.18.3.525

Lu X, Liu YJ, Sun LP (2020) Influence of initial imperfections on post buckling strength of concrete filled rectangular steel tubular column panels. *Journal of Architectural Science and Engineering* 37(5):170-181, DOI: 10.19815/j.jace.2020.09044 (in Chinese)

Park JW (2010) Behaviors of concrete filled square steel tubes confined

by carbon fiber sheets (CFS) under compression and cyclic loads. *Steel and Composite Structures* 10(2):187-205, DOI: 10.12989/scs.2010.10.2.187

Sundarraja MC, Ganesh PG (2010) Experimental study on CFST members strengthened by CFRP composite under compression. *Journal of Constructional Steel Research* 72(5):75-83, DOI: 10.1016/j.jcsr.2011.10.014

Sundarraja MC, Ganesh PG (2011) Finite element modeling of CFRP jacketed CFST members under flexural loading. *Thin-Walled Structures* 49(12):1483-1491, DOI: 10.1016/j.tws.2011.07.008

Tao Z, Han LH, Zhuang JP (2007) Axial loading behavior of CFRP strengthened concrete-filled steel tubular stub columns. *Advances in Structural Engineering* 10(1):37-46

Tao Z, Wang ZB, Han LH, Yu B (2011) Fire performance of concrete-filled steel tubular columns strengthened by CFRP. *Steel and Composite Structures* 11(4):307-324, DOI: 10.13577/j.jnd.2015.0207 (in Chinese)

Wang QL, Li J, Shao YB (2015) Flexural performances of square concrete filled CFRP-steel tubes (S-CF-CFRP-ST). *Advances in Structural Engineering* 18(8):1319-1344, DOI: 10.1260/1369-4332.18.8.1319

Wang QL, Qu SE, Shao YB, Feng LM (2016) Static behavior of axially compressed circular concrete filled CFRP-steel tubular (C-CF-CFRP-ST) columns with moderate slenderness ratio. *Advanced Steel Construction* 12(3):263-295, DOI: 10.18057/ijasc.2016.12.3.4

Wang QL, Shao YB (2014) Compressive performances of concrete filled square CFRP-steel tubes (S-CFRP-CFST). *Steel and Composite Structures* 16(5):455-480, DOI: 10.12989/scs.2014.16.5.455

Wang QL, Shao YB (2015) Flexural performance of circular concrete filled CFRP-steel tubes. *Advanced Steel Construction* 11(2):127-149, DOI: 10.18057/ijasc.2015.11.2.1

Yao W (2006) Orthogonal experimental study on the effect of concrete mix proportion on shrinkage. *Journal of Building Materials* 1(1):92-98, DOI: 10.3969/j.issn.1007-9629.2006.01.017 (in Chinese)

Zand AW, Badaruzzaman WHW, Mutalib AA, Hilo SJ (2016) The enhanced performance of CFST beams using different strengthening schemes involving unidirectional CFRP sheets: An experimental study. *Engineering Structures* 128(1):184-198, DOI: 10.1016/j.engstruct.2016.09.044

Zand AW, Badaruzzaman WHW, Mutalib AA, Hilo SJ (2017) Rehabilitation and strengthening of high-strength rectangular CFST beams using a partial wrapping scheme of CFRP sheets: Experimental and numerical study. *Thin-Walled Structures* 114(1):80-91, DOI: 10.1016/j.tws.2017.01.028